Computational analysis of the indirect combustion noise generation mechanism in a nozzle guided vane in transonic operating conditions

Alessandro Ceci [a,*], Romain Gojon [a,b], Mihai Mihaescu [a]

[a] *KTH Royal Institute of Technology, Competence Center for Gas Exchange (CCGEx) Sweden*
[b] *ISAE-SUPAERO, Université de Toulouse, France*

ABSTRACT

The combustion noise in modern engines is mainly originating from two types of mechanisms. First, chemical reactions in the combustion chamber leads to an unsteady heat release which is responsible of the direct combustion noise. Second, hot and cold blobs of air coming from the combustion chamber are advected and accelerated through turbine stages, giving rise to entropy noise (or indirect combustion noise). In the present work, numerical characterization of indirect combustion noise of a Nozzle Guide Vane passage was assessed using three-dimensional Large Eddy Simulations. The present work offers an overview to the analytical, computational and experimental studies of the topic. Numerical simulations are conducted to reproduce the effects of incoming planar entropy waves from the combustion chamber and to characterize the generated acoustic power. The dynamic features of the flow are addressed by the means of frequency domain and modal analyses techniques such as Fourier Decomposition and Proper Orthogonal Decomposition. Finally, the predicted entropy noise from numerical calculations is compared with the analytical results of an actuator disk model for a stator stage. The present paper proves that the generated indirect combustion noise can be significant for transonic operating conditions. The blade acoustic response is characterized by the excitation of a latent dynamics at the forcing frequency of the planar entropy waves, and it increases as the amplitude of the incoming disturbances increases.

1. Introduction

Indirect combustion noise was early investigated in the works of Candel [1] and Marble and Candel [2]. They proposed an analytical model for the convection of non-uniform temperature regions through a nozzle in several configurations: subsonic, supersonic and supersonic with shocks in the divergent segment. Compared to the real three-dimensional flow phenomenon, the model assumes quasi-one-dimensional inviscid flow and compactness of the nozzle (i.e. the length of the incoming

disturbances is much larger than the nozzle length). The relations linking the different perturbations are established using only conservation laws. In supersonic operations, the critical mass-flow is also imposed at the throat.

A definitive analytical model of indirect combustion noise for any geometry and disturbance type is still missing in literature [3]. Developments have been made by Howe [4] who transformed the momentum equation in Crocco's form into an acoustic analogy equation and found a solution to the non compact nozzle problem using a Green function. In his work, he also took into account the noise contribution from the separated flow in the divergent section.

Further analyses by Goh and Morgans [5] proposed an extension of the compact assumption, proposing an alternative approach which derives *effective lengths* for the passage of the flow through a supercritical convergent-divergent nozzle. Another model extension was developed by Duran and Moreau [6], which computed the nozzle response through an asymptotic expansion of the linearised Euler equations, using Magnus expansion. Compositional inhomogeneities in the gas mixture have been also examined by Magri et al. [7], who computed subcritical and supercritical nozzle responses, comparing the contribution of compositional noise to entropy noise and direct noise; it was found that compositional noise can exceed entropy noise for supercritical nozzles and fuel-lean conditions.

From an experimental point of view, an extensive study of entropy noise has been carried out by Bake et al. [8]. The experimental device consists of a straight tube flow with a heating module and a nozzle where the flow is accelerated. This apparatus is well known as the Entropy Wave Generator (EWG) and several numerical investigation of the EWG experiment can be found in literature. The results showed that the pressure signals obtained in the EWG experiment come from two main mechanisms: the entropy-to-acoustic conversion of the perturbations via strong mean velocity gradients in the nozzle, including the presence of shocks in the nozzle, and the acoustic reflection at the exhaust due to the non perfect anechoic outlet.

Studies have also shown that in compact premixed combustors of low-emission systems, acoustic oscillations and entropy fluctuations interact with each other, with entropy waves coupling constructively as well as destructively with combustor acoustics [9].

In 1977 Cumpsty and Marble [10] proposed an analytical method, based on the actuator disk theory, for the evaluation of indirect combustion noise through several turbine stages. It is based on the axial compactness assumption for the blade geometry (analogously to the nozzle) but it considers a 2D configuration taking into account the flow deflection due to the circumferential velocity component of the blades, which induces vorticity fluctuations.

Leyko et al. [11] analysed the wave generation and transmission mechanism from a numerical perspective. In their work they accessed the range of validity of the compact assumption for a stator blade row, comparing the analytical results with simulations data. The incoming disturbances used in the simulations were planar 1D temperature pulses and the acoustic response of the row was evaluated. In the numerical simulations, planar entropy waves were shown to be strongly distorted in the inter blade passage at high frequencies. An extensive experimental study was recently conducted in the high pressure turbine facility at Politecnico di Milano in the framework of the European funded project RECORD (Research on Core Noise Reduction) [12]. Two turbine operating conditions were investigated, subsonic and transonic respectively. The entropy wave excitation was shown to generate additional acoustic power correlated to the temperature amplitude of the incoming disturbances.

The objective of this paper is to conduct accurate Large Eddy Simulations (LES) through a simplified transonic Nozzle Guide Vane (NGV) stage of a high pressure turbine in order to gain insights and explanation of the entropy to noise conversion mechanism. Pure entropy waves of different wavelengths are injected in the computational domain and the acoustic response of the blade passage is evaluated downstream.

The Fourier decomposition of the pressure fluctuation field highlights region of high pressure waves' amplitude, which are not present in the case of non injected entropy waves. Proper Orthogonal Decomposition (POD) analyses, on the other hand, identify the most coherent structures in the flow-field containing high energy modes.

The present work shows that the entropy to acoustic wave conversion mechanism is of great importance and it offers a parametric study related to the wavelengths of the incoming disturbances.

Transonic conditions are characterized by trailing edge expansion and compression waves and it is shown that their dynamics are affected by injecting inlet disturbances with a particular tone. It is possible to observe that, once entropy waves are injected in the domain, on the suction side of the blade both acoustic responses and POD modes are excited by the particular frequency of disturbances.

Finally, the comparison of results with the ones from an analytical model highlights the differences between the two approaches.

2. Methodology

2.1. Geometry, computational domain, and mesh

The geometry considered in the present study is a simplified topology of a real NGV passage based on experimental and numerical studies conducted by Yasa et al. [13,14]. The experiments were conducted in the KTH transonic test tunnel facility.

The description of the facility is clearly addressed in the work of Yasa et al. [13]. The NGV design parameters of interest for the present study are the axial chord $C_{ax,mid}$ at mid-span, the trailing edge diameter d and the blade to blade distance at mid-span H, where the blade to blade distance represents the pitchwise distance at midspan from the leading edges of two

Table 1
NGV main parameters.

Parameter	Value	Unit
$C_{ax,mid}$	0.0657	m
d	0.0022	m
H	0.08345	m
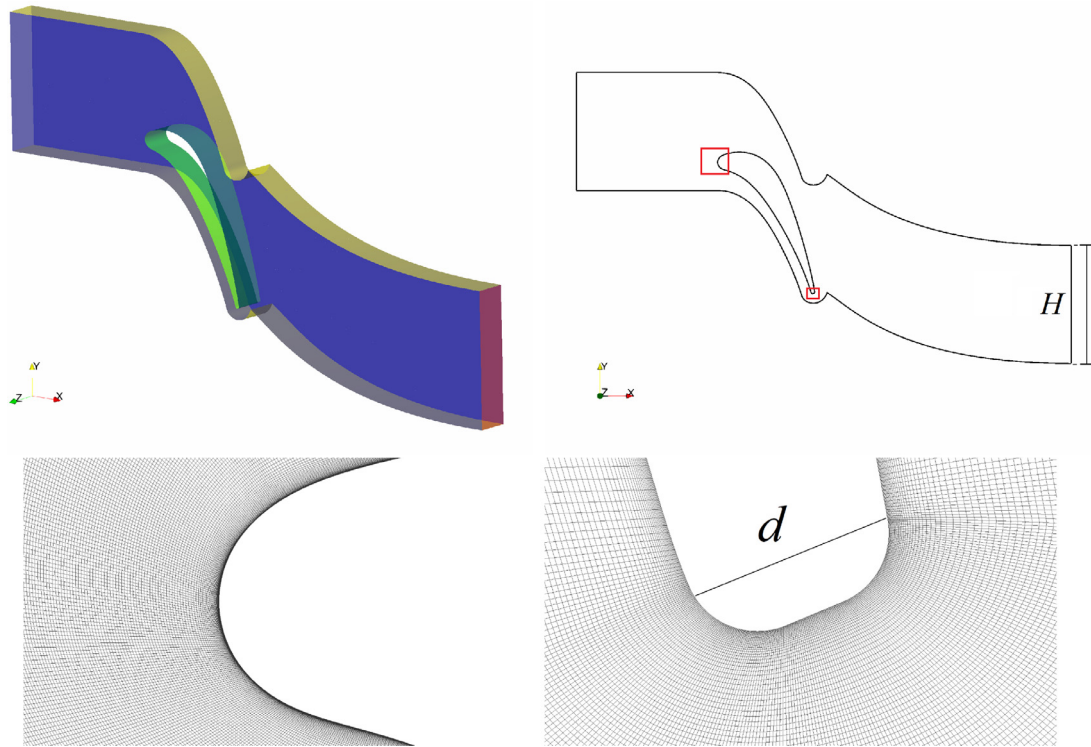
Fig. 1. 3D geometry (z-depth magnified 100 times for clarity) and simplified 2D mid-section of the computational domain, together with mesh details (highlighted red boxes). (For interpretation of the references to colour in this figure legend, the reader is referred to the web version of this article.)

consecutive blades. These parameters are summarized in Table 1. The operating conditions of the vane have been assessed by looking at different measurements at specific inlet and outlet locations [13].

In this study, the baseline case refers to previous results by Ceci et al. [14], with the aim of reproducing a simplified set-up of the study conducted in the experiments, without any temperature fluctuations injected at the inlet. The simplified model is a two-dimensional section of the blade geometry at mid-span, extruded spanwise in the third direction. The computational domain, together with leading and trailing edges mesh details, are visible in Fig. 1. In order to apply azimuthal periodic boundary conditions, the height of the computational domain is exactly equal to the blade to blade distance H.

The numerical simulations are carried out solving the compressible Navier Stokes equations with a density based solver, with a sub-grid scale LES model for the turbulent kinetic energy. The computational grid counted about 55.5 million volume cells. Grid stretching at the inlet and outlet of the domain was adopted in order to eliminate spurious reflections. Throughout the paper, the term baseline refers to the unforced numerical simulation at the inlet temperature $T_1 = 303.15$ K.

For a complete overview of the mesh parameters, boundary conditions, numerics and validation efforts carried out with respect to this case, the reader is directed to Ceci et al. [14].[1]

2.2. General flow features

The flow is subsonic at the inlet of the domain and the local Mach number is equal to $M_1 = 0.15$. Then the flow is accelerated up to sonic condition at the throat of the nozzle guided vane passage (at $x/C_{ax,mid} \approx 0.75$). Passed the throat, the flow interacts with compression and expansion waves emitted from the shed vortices at the trailing edge, as shown in Fig. 2. These waves are also impinging on the suction side of the blade and then are reflected back towards the normal

---

[1] https://doi.org/10.1007/s10494-018-9964-9.

div(U) (1/s)

-5000   -2500   0   2500   5000

U Magnitude (m/s)

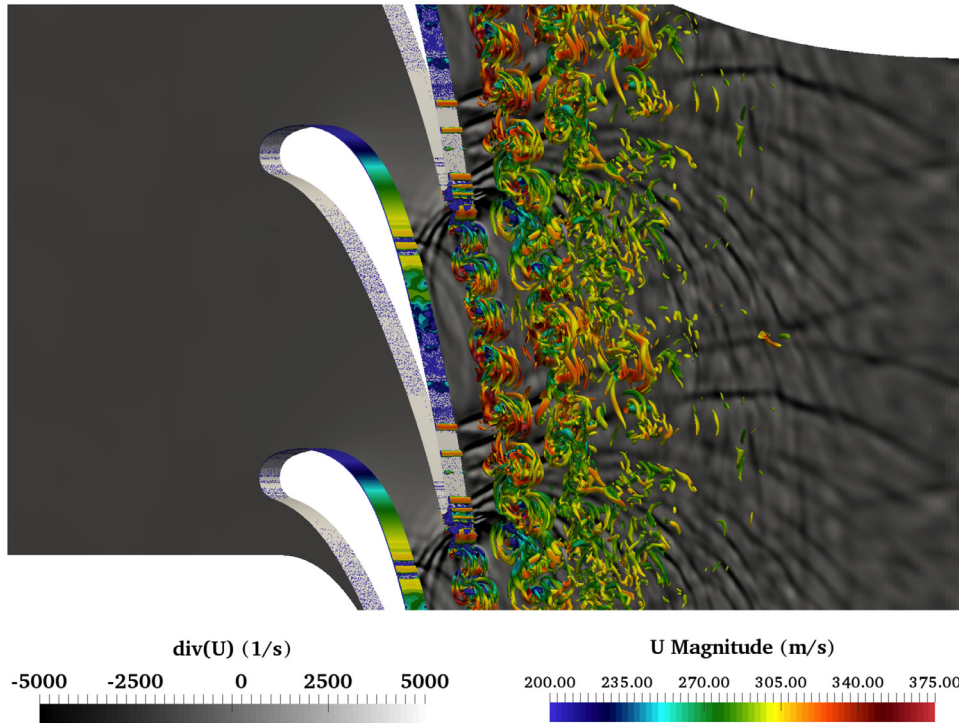200.00   235.00   270.00   305.00   340.00   375.00

Fig. 2. Isocontours of Q-criterion (coloured with the velocity magnitude) superimposed on the divergence of the velocity field.

direction of the surface. The flow accelerates further on the suction side due to a Prandtl-Mayer expansion. Almost at the end of the suction side, it is possible to observe compressibility effects: a system of weak shocks interacting with the wake is present throughout the final part of the suction side. By looking at the animation corresponding to Fig. 2, it seems that the system of weak shocks is moving with a characteristic dynamics.

2D organised vortices can be seen from the rounded trailing edge to an axial distance corresponding to $x/C_{ax,\text{mid}} = 0.2$ downstream the blade, then the overall two-dimensional organization starts to break down in smaller and less organized eddies.

The shedding frequency predicted by the 3D LES is of $f_s = 24$ kHz, corresponding to a Strouhal number of $St_s = f_s d/U = 0.176$. The Strouhal number is calculated with the length scale $d = 0.0022$ m being the trailing edge diameter and the velocity scale U being equal to the one calculated from the exit Mach number of 0.95. The experimental shedding frequency was found to be $21 - 22$ kHz for transonic/supersonic operating conditions [13].

3. Impact of forced inlet temperature fluctuations

A similar numerical setup to the baseline case is adopted for the forced ones. Hot and cold spots of air are imposed as a planar sinusoidal wave train at the inlet plane of the computational domain. The aim is to observe the entropy to acoustic conversion of inflow disturbances through the NGV passage. The frequency content and the acoustic response of the blade row are analysed in order to observe the effects of the forcing. Then, the effect of increasing the inlet temperature is studied with the aim of simulating more realistic scenarios and to address the effects on the NGV acoustic response. The forcing wave has characteristic temporal frequency $f_1 = 1000$ Hz and amplitude $A = 4.8\%$, according to

$$\tilde{T}_1 = T_1[1 + A\sin(2\pi f_1 t)] \tag{1}$$

For a more comprehensive reading of the forced case at the temperature $T = 303.15$ K, the reader is again redirected to the results found in [14].

The parametric study has been conducted in terms of changing the reference inlet static temperature. The numerical setup is identical for all the forced simulations, with the temperatures changing accordingly to the desired case to simulate. In addition, the specific heat ratio γ and the specific heat at constant pressure c_p is always kept constant during the simulation, but with their values based on the selected inlet static temperatures. The other two analyses have been performed, respectively, with inlet temperatures equal to $T_1 = 600$ K and $T_1 = 900$ K.

In all simulated cases, the Mach numbers M_1 and M_{2is} always kept their values of 0.15 and 0.95 respectively. The reference velocity of the Strouhal number hence changed, since sonic conditions are based on different total temperatures and velocity scales derived from $M_{2is} = 0.95$.

Table 2
Forced simulations parameters.

T_1, K	A	f_1, Hz	$\lambda_s/C_{ax,\text{mid}}$	u_1, m/s	t^*
303.15	4.8%	1000	0.76	51.90	7.60
600	4.8%	1000	1.11	73.02	11.11
900	4.8%	1000	1.36	89.43	13.61

(a)

(b)   (c)

T/T1

0.785   0.840 0.880 0.920 0.960 1.000   1.048
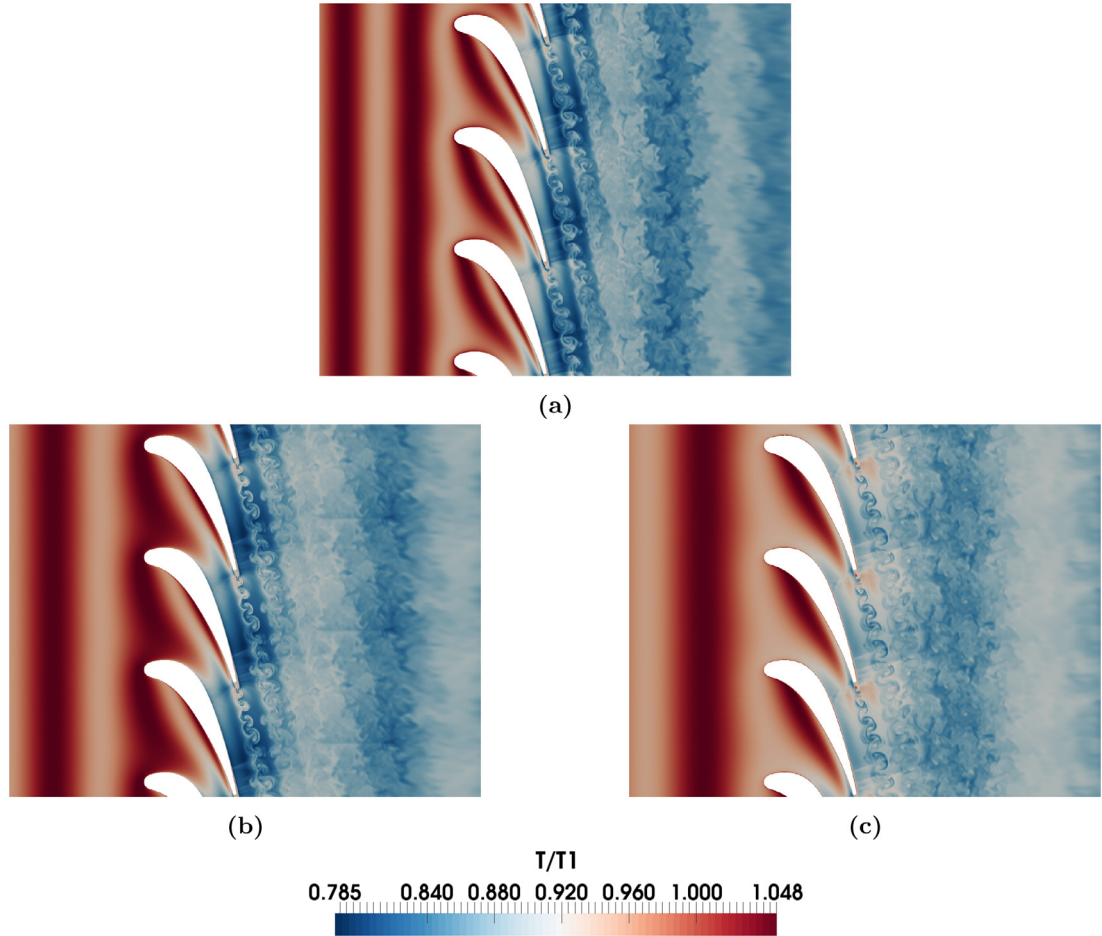
Fig. 3. Instantaneous static temperature ratio T/T_1; forced inlet temperature $T_1 = 303.15$ K (a), $T_1 = 600$ K (b) and $T_1 = 900$ K (c).

In this manner it is also possible to evaluate the effects of different wavelengths of the incoming entropy waves. The present parametric study assesses the different acoustic production mechanisms as functions of the ratio $\lambda_s/C_{ax,\text{mid}}$, with λ_s being the wavelength of the injected entropy wave. The physical simulated time for the forced simulation is equal to 0.01 (s), corresponding to 10 cycles at the forcing frequency f_1. A non-dimensional time scale is defined as $t^* = u_1 t/C_{ax,\text{mid}}$, where u_1 is computed from the relation $M_1 = u_1/c_1$, being c_1 the inlet speed of sound. The forced simulations characteristics are specified in Table 2. For the choice of the particular forcing frequency of 1000 Hz, the reader is invited to consult the Methodology section of [14]. A key reason is the high computational cost of the 3D LES, i.e. conducting all the simulations of the parametric study for a forcing frequency one order of magnitude smaller, would have been too demanding in terms of resources.

Fig. 3 shows the static temperature ratio T/T_1 for the three forced simulations. At the inlet of the computational domain, the vertical stripes highlight the different wavelengths of the entropy waves, given by the dispersion relation $\lambda_s = M_1 c_1/f_1$. The wavelengths normalized by the axial chord $C_{ax,\text{mid}}$ are then: $\lambda_s/C_{ax,\text{mid}}|_{303.15[K]} = 0.76$, $\lambda_s/C_{ax,\text{mid}}|_{600[K]} = 1.11$ and $\lambda_s/C_{ax,\text{mid}}|_{900[K]} = 1.36$. It is also possible to observe that these waves tend to return to their planar organization downstream of the vane for all cases. The wake region seems also to be thicker for higher inlet temperatures.
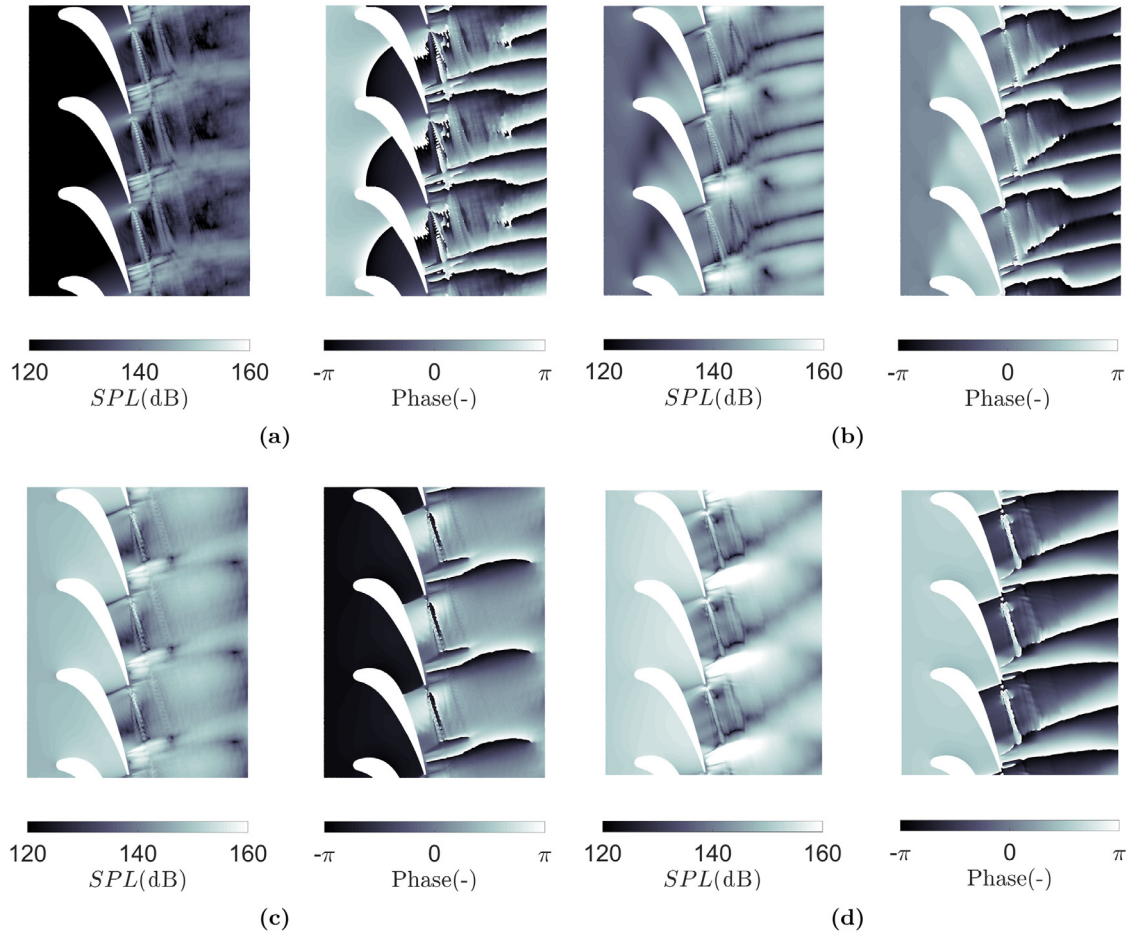
Fig. 4. Amplitude (left) and phase (right) of the FFT of the pressure fluctuation field at f_1; baseline case $T_1 = 303.15$ K (a), forced inlet temperature $T_1 = 303.15$ K (b), $T_1 = 600$ K (c) and $T_1 = 900$ K (d), reference pressure $p_{ref} = 20\ \mu$Pa.

3.1. Fourier decomposition of fluctuation fields

The Fourier transform of the two dimensional snapshots, at the inlet forcing frequency f_1 is computed for temperature and pressure fields. The number of snapshots is equal to 1800. The sampling frequency was equal to four times the vortex shedding one.

Please note that, adequate sampling frequencies are used, for higher temperatures, in order to avoid aliasing and assuming a constant Strouhal (≈ 0.2) number associated with the shedding frequency.

3.1.1. Pressure fluctuations

For the pressure fluctuations field p', the amplitude and the phase fields of the baseline unforced case, at the frequency f_1, are shown in Fig. 4. In the present work, the amplitude field of the pressure fluctuations and future computations of sound pressure levels are expressed in decibels, dB, taking as reference pressure the value $p_{ref} = 20\mu$ Pa.

For the unforced simulation (Fig. 4a), it is possible to observe the presence of a system of compression and expansion waves (towards the trailing edge, suction side) moving at a frequency of 1000 Hz. The phase field of the pressure fluctuations field shows the spatial periodicity of the flow. The amplitude of the pressure fluctuations is negligible upstream of the NGV passage, up to the throat section, as there are no imposed entropy waves in this case.

It can be observed that the amplitude of the pressure fluctuations is increasing in the blade trailing edge region from the unforced case (Fig. 4a) to the forced ones (Fig. 4b–d), suggesting a stronger motion of the weak shocks at this frequency. This stronger motion of the shocks leads to an acoustic emission in the downstream direction.

The case at $T_1 = 900$ K presents very high pressure field amplitudes in such a zone, as it can be visualized from Fig. 4d. The interaction of the entropy waves with the acoustic field created at f_1, becomes more and more important as the inlet static temperature increases. Moreover, the *SPL* in the converging portion of the vane and upstream of the blade increases as
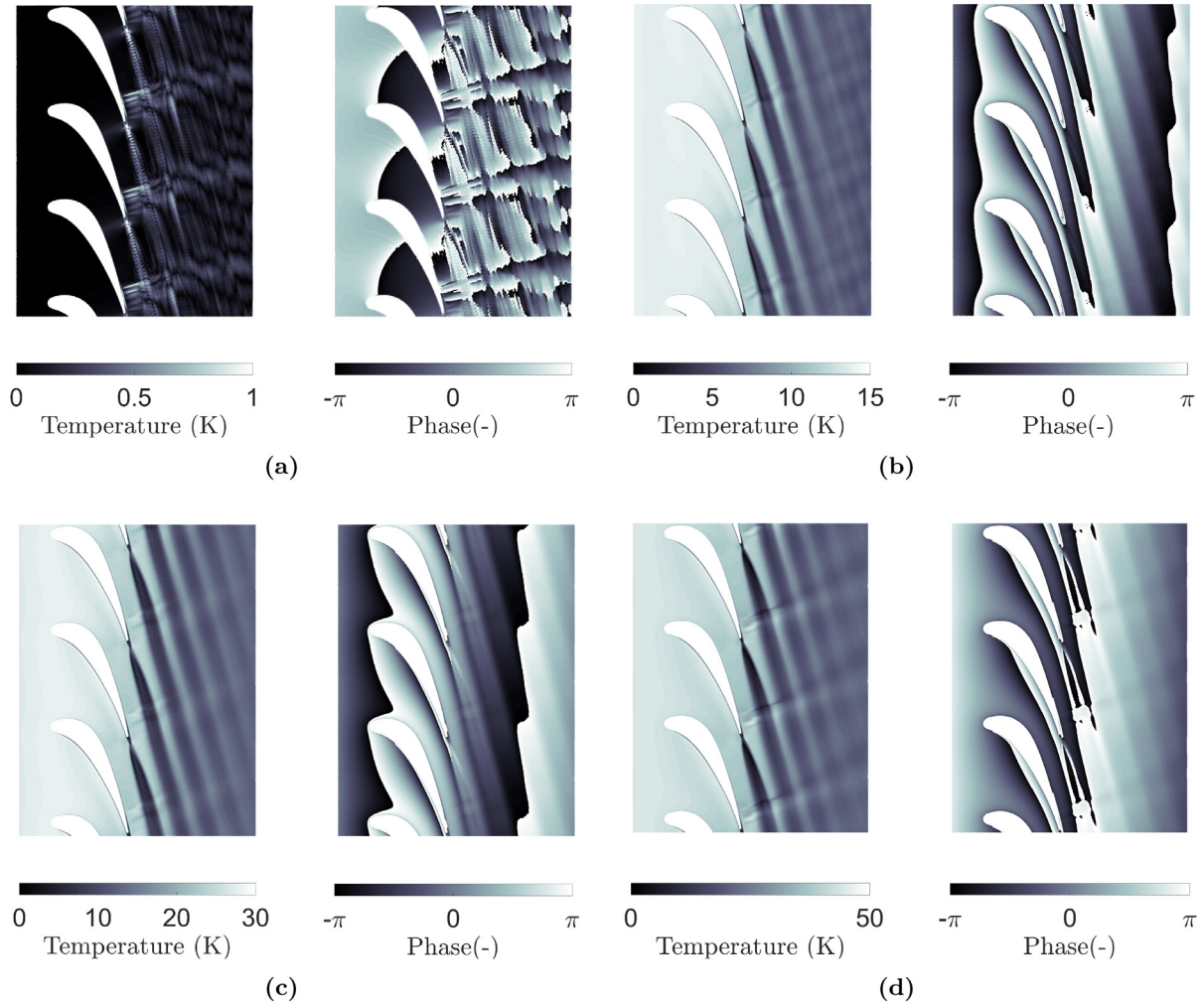
Fig. 5. Amplitude (left) and phase (right) of the FFT of the temperature fluctuation field at f_1; baseline case $T_1 = 303.15$ K (a), forced inlet temperature $T_1 = 303.15$ K (b), $T_1 = 600$ K (c) and $T_1 = 900$ K (d).

well, in accordance with the aforementioned trend. This result suggests that the entropy-to-acoustic conversion mechanism is enhanced when increasing the inlet temperature.

The phase fields of the pressure fluctuation downstream of the blade are similar, with sharp changes of phase identifying wavefronts.

3.1.2. Temperature fluctuations

For the temperature field, the same low frequency dynamics as for pressure is visible in the amplitude field of the unforced case, Fig. 5a.

The amplitude field of the forced simulation (Fig. 5b) shows that entropy waves reduce their intensity after passing the blade row. The interaction with the system of shocks is also visible. On the other hand, the forced phase field at the same frequency shows the planar character of the incoming entropy waves, which are not organised in any particular manner at unforced conditions. Afterwards, the planar waves get strongly distorted through the NGV passage and "*streaks*"-like structures are visible in the middle of the passage. Those waves return almost planar approximately one axial chord $C_{ax,\text{mid}}$ downstream of the blade row.

As inlet temperature increases, Fig. 5c and d, the features of the amplitude field are similar, with an increasing width of the wake region. The maximum amplitude magnitude divided by its respective inlet temperature is 4.8% since the maximum temperature is registered at the inlet, where the forcing is imposed.

The phase field identifies, instead, the planar character of the incoming entropy waves which are then distorted and finally propagated downstream. The wavelength of the planar waves also increases with respect to the inlet temperature.
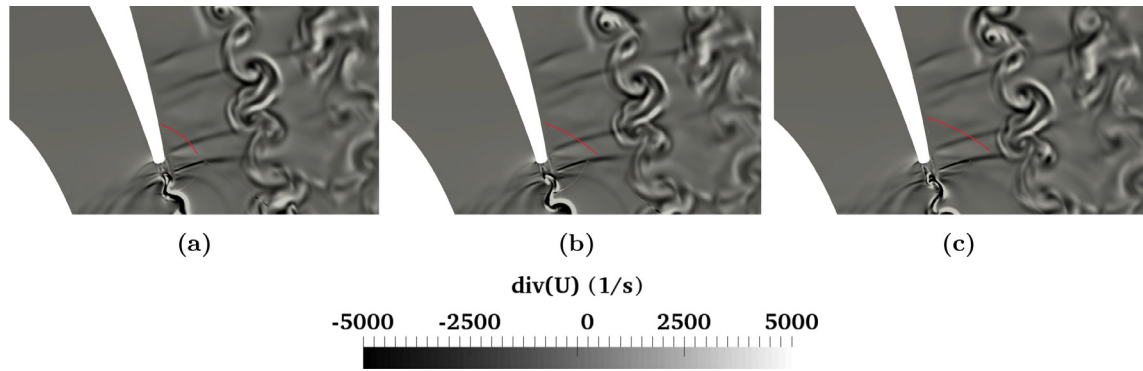
Fig. 6. Instantaneous divergence field div(U) at three instants of time (a), (b), (c) (from left to right); forced inlet temperature $T_1 = 303.15$.

In conclusion, the presence of acoustic production at the forcing frequency f_1, with noticeable amplitudes, is observed both upstream and downstream of the blade passage. The downstream generated noise seems to be emitted from the system of weak shocks on the suction side, as the trailing edge weak shocks are already moving at a frequency of 1000 Hz in the unforced case (Fig. 4a). When entropy waves are imposed ar the inlet, the blade acoustic response is also characterised by the excitation of a latent dynamic of the unforced case at 1000 Hz. It seems that the weak shock movement is "locked in" at this particular frequency, due to the presence of the forcing.

Fig. 6 shows the divergence of the velocity field for the forced case at $T_1 = 303.15$ K at three time instants. The system of weak shocks on the suction side of the blade can be recognised by the dark areas of the div(U) field, while the acoustic waves are highlighted by the red curves.

The upstream noise is generated in the subsonic convergent region of the passage and then reflected backwards. No perturbation of the shedding dynamics is induced by the inlet forcing, this result may be due to the very different frequencies of the two phenomena.

3.2. Proper orthogonal decomposition analysis

In the present subsection, *Proper Orthogonal Decomposition* (snapshot POD method [15]) is used in order to extract the most relevant modeshapes appearing in the 2D snapshots sampled at mid-span during the simulations. The number of snapshots is equal to 1800. Study is performed for the unforced and forced flow-fields. The resulting non-dimensional eigenvectors (*topos*) forms an orthonormal basis. Therefore the colorscale of POD results presented in this paper (from black to white) ranges the values from -0.003 to 0.003. These are chosen in order to identify more clearly the features of each modeshape.

Throughout the paper, the ith chrono-mode a_i frequency content is expressed in terms of the Strouhal number with the usual definition $St = fd/U$, while its time history in terms of time t expressed in seconds. The main St numbers the authors refer to are the ones associated to the shedding frequency f_s and forcing frequency f_1, reminding that the velocity used for the St computation is the one calculated from the vane exit Mach number of 0.95.

3.2.1. POD analysis, pressure field at unforced inlet conditions

The analysis is focused on the pressure fluctuation field p', for which the POD algorithm is applied. The energy associated to each mode is plotted in Fig. 7.

The appearance of modes as a couple is an evidence that the modes represent a wave-like periodic structure of the flow: POD modes are represented by real functions, and two modes are needed to describe a travelling wave, representing the real and complex parts respectively.

The first couple of modes, associated with the shedding phenomenon, contains 17% of the total energy, while the energy content per mode drops below 5% for the successive ones. To represent 90% of the total energy, approximately 300 modes are needed. The modeshape associated with the vortex shedding is pictured in Fig. 8a; once again the dominant tone is at $St = 0.176$, i.e approximately 24 kHz. The couple $3 - 4$ is associated with the system of compression and expansion waves arising from the trailing edge, as depicted in Fig. 8b. It is possible to observe that, even without the presence of the forcing, the frequencies of this movement are in a range from $500 - 3000$ Hz, i.e. in the St range of $0.00367 - 0.02199$. This feature, underlines the presence of flow dynamics in the low frequency range.

Other couples are also associated with the low frequency dynamics of the compression and expansion waves originating from the trailing edge and are analogous to the temperature topo-modes.

3.2.2. POD analysis, pressure field at forced inlet conditions

Looking at the POD of forced cases, additional modes which were not present in the baseline case are found. For $T_1 = 303.15$ K at the dominant tone $St_1 = 0.00733$, two new topo-modes appear. The first couple of POD modeshapes is still
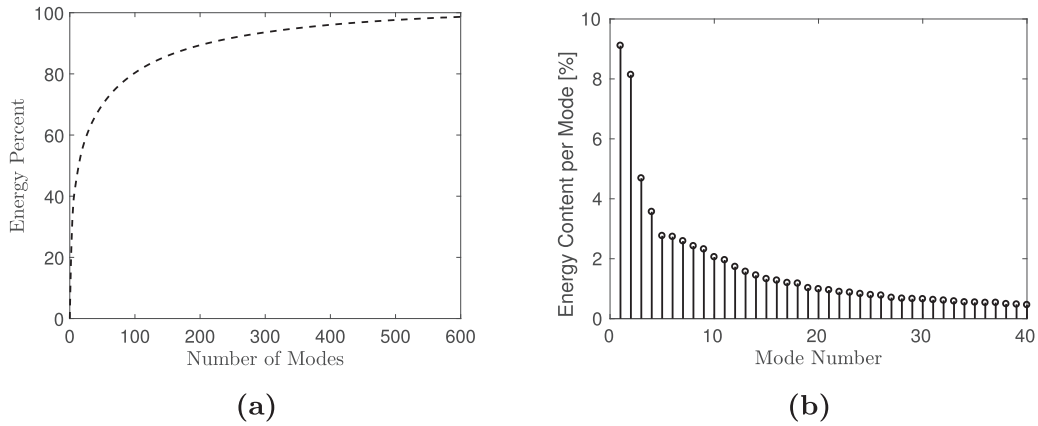
Fig. 7. Cumulative energy percent retaining the first 600 modes (a), and energy associated to each mode (b). Pressure fluctuation field p'; baseline case $T_1 = 303.15$ K.
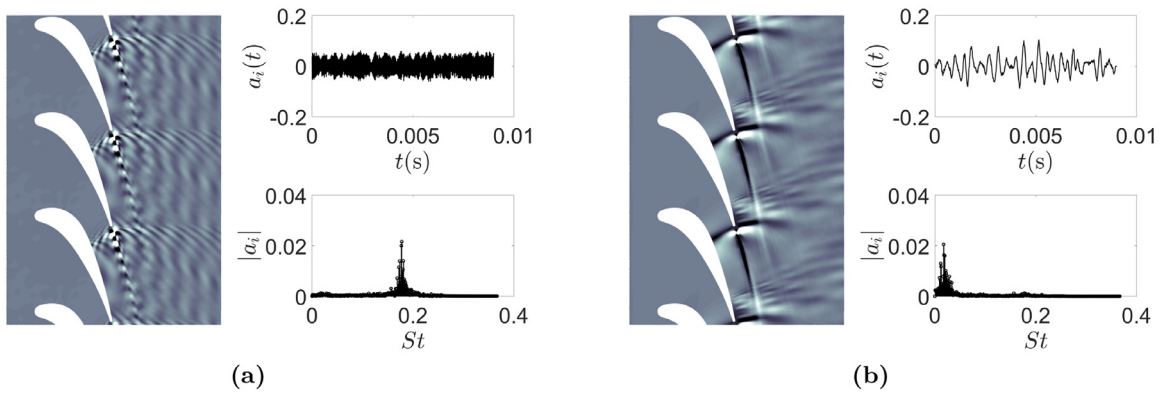

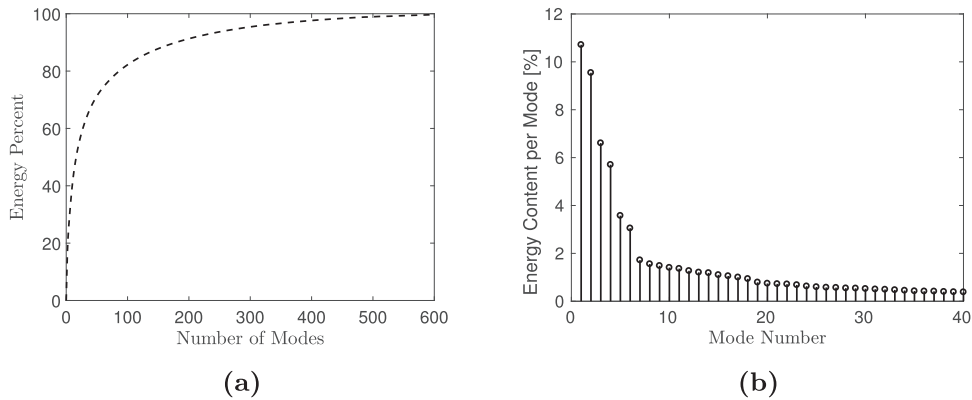**Fig. 8.** First (a) and third (b) POD mode of the pressure fluctuation field p'; baseline case $T_1 = 303.15$ K.


Fig. 9. Cumulative energy percent retaining the first 600 modes (a), and energy associated to each mode (b). Pressure fluctuation field p'; forced inlet temperature $T_1 = 303.15$ K.

associated with the shedding phenomenon, but the couple $3 - 4$ exhibits now a topo-mode at the inlet forcing frequency f_1, associated with the shock movement. The temporal trend can be clearly visualized from the time history of the associated temporal coefficient in Fig. 10. The chrono-mode is clearly characterized only by the forcing frequency f_1, underlining a strong correlation between the topo-mode and the presence of the forcing. The shedding mode is instead identical to the unforced case. The ratio between the shedding St numbers is $St_s/St_1 = 0.176/0.00733 \approx 24$.

The energy content of the POD for the forced case is shown in Fig. 9. Now, the first 6 modes contain 38% of the total energy as compared to the 30% of the baseline case, with the couple $3 - 4$ retaining 12% of it. The pressure fluctuations POD
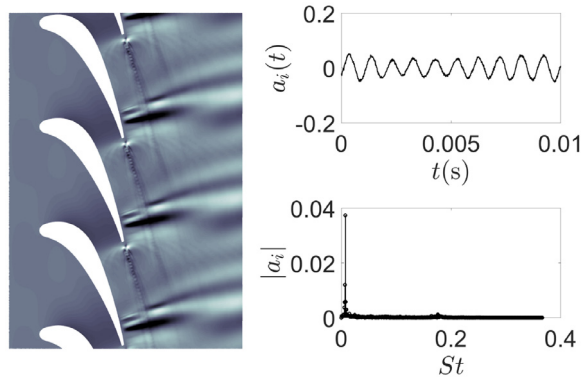
Fig. 10. Third POD mode of the pressure fluctuation field p'; forced inlet temperature $T_1 = 303.15$ K.
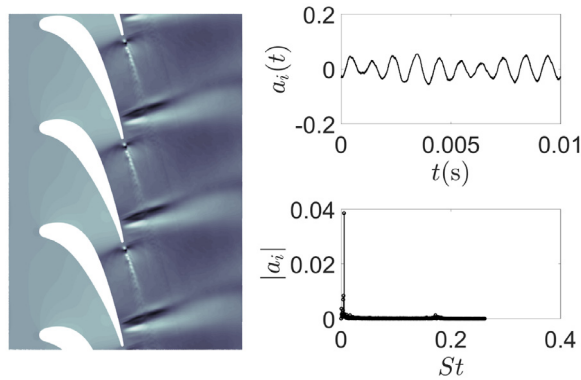
Fig. 11. Third POD topo-mode of the pressure fluctuation field associated to the dominant frequency f_1; forced inlet temperature $T_1 = 600$ K.

at higher inlet forcing temperatures, instead, is more complex and less straight forward to interpret. This is due to the fact that some topo-modes appear mixed to other frequencies.

For the intermediate wavelength ratio $\lambda_s/C_{ax,\mathrm{mid}} = 1.11$ ($T_1 = 600$ K), the first four modes are always associated with the shedding phenomenon and with the presence of coherent flow structures at the forcing frequency f_1. They contain 24% of the total energy and the individual modes are not always associated to a single temporal frequency.

This aspect can be seen in Fig. 11, which clearly depicts the characteristic modeshape of the pressure fluctuations field at $f_1 = 1000$ Hz mixed to a small frequency content of the shedding at f_s. The shedding St number at $T_1 = 600$ K remains very close to the one for $T_1 = 303.15$ K, being equal to $St_s = 0.173$. The St number at the forcing frequency is now $St_1 = 0.00524$, hence the ratio $St_s/St_1 = 0.173/0.00524 \approx 33$. Some spatial features related to vortex shedding are visible in the topo-mode. In addition, there is also a small peak at the shedding frequency in the spectrum of the chrono-mode. The energy content per mode is similar to the one in Fig. 9 at $T_1 = 303.15$ K.

For the largest wavelength $\lambda_s/C_{ax,\mathrm{mid}} = 1.36$ ($T_1 = 900$ K), instead, the association of a single topo-mode to multiple temporal frequencies becomes even stronger than the previous case. There are, again, two modes which are prevalently linked to the shedding frequency $St_s = 0.16$, but they exhibit a noticeable tone at the frequency $St_1 = 0.00431$. These modes can be visualized in Fig. 12. The same situation happens for the topo-modes mainly associated with the forcing frequency $St_1 = 0.00431$. The mode in Fig. 12b shows a clear peak at $St_s = 0.16$, in addition to the one at $St_1 = 0.00431$. The St number ratio for the largest wavelength case is $St_s/St_1 = 0.16/0.0431 \approx 37$.

The energy content associated to the first four mode is around 55%, with the topo-modes associated with f_1 retaining 25% of it. All the remaining modes exhibit energy contents per mode below 2%.

It can be noted, again, that single odd modes are depicted due to the appearance as a couple.

In conclusion, the POD analysis at all inlet temperatures, despite suffering of mixed frequency content inside a modeshape at the largest temperature, is able to identify additional modes with characteristic shape at f_1, which were absent in the baseline case.

### 3.2.3. POD analysis, temperature field at unforced inlet conditions

From the modeshapes' analysis of the temperature, it is immediately possible to recognize the different features characterizing the unforced and the forced cases. The cumulative energy distribution among the temperature fluctuation modes, is shown in Fig. 13 for the baseline case. One can see that the first 8 modes roughly capture 20% of the energy, with mode 1
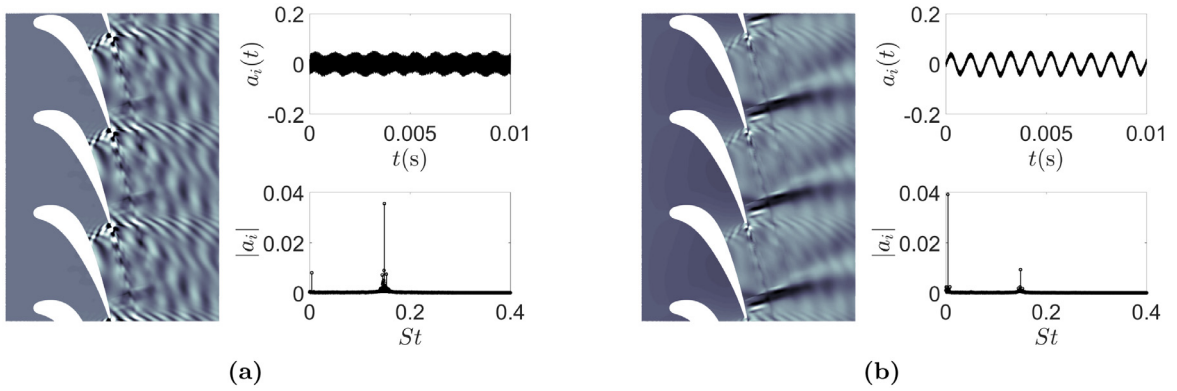
Fig. 12. First (a) and third (b) POD topo-modes of the pressure fluctuation field associated to the vortex shedding at frequency f_s; forced inlet temperature $T_1 = 900$ K.
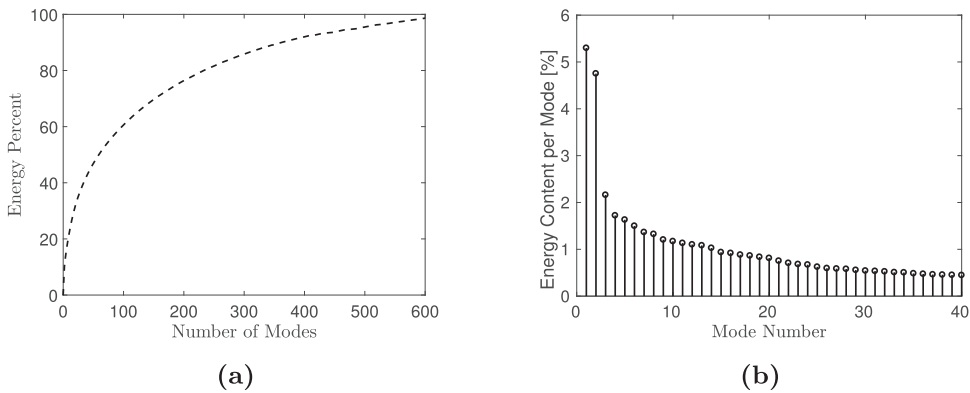
Fig. 13. Cumulative energy percent retaining the first 600 modes (a), and energy associated to each mode (b). Temperature fluctuation field T'; baseline case $T_1 = 303.15$ K.
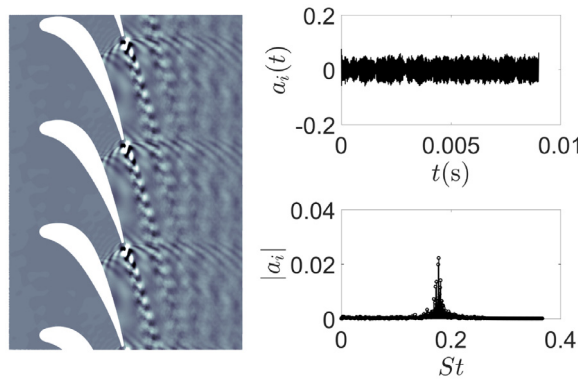
Fig. 14. First POD mode of the temperature fluctuation field T'; baseline case $T_1 = 303.15$ K.

and 2 containing the highest energy content per mode $\approx 5\%$. In order to capture 90% of the energy, 400 modes are needed. An analysis of the chrono- and topo-modes showed that the first two POD modes have a similar periodicity (frequency content) and a similar structure in space.

The first POD mode is represented in Fig. 14. The dominant frequency is $St = 0.176$ as shown in the chrono-modes of Fig. 14.

From a physical point of view, these structures represent the vortex shedding phenomenon. It is also possible to observe the acoustic waves which are generated by the vortices at the trailing edge of the blade.

Once again, POD modes are depicted in single pictures due to their appearance as couples.
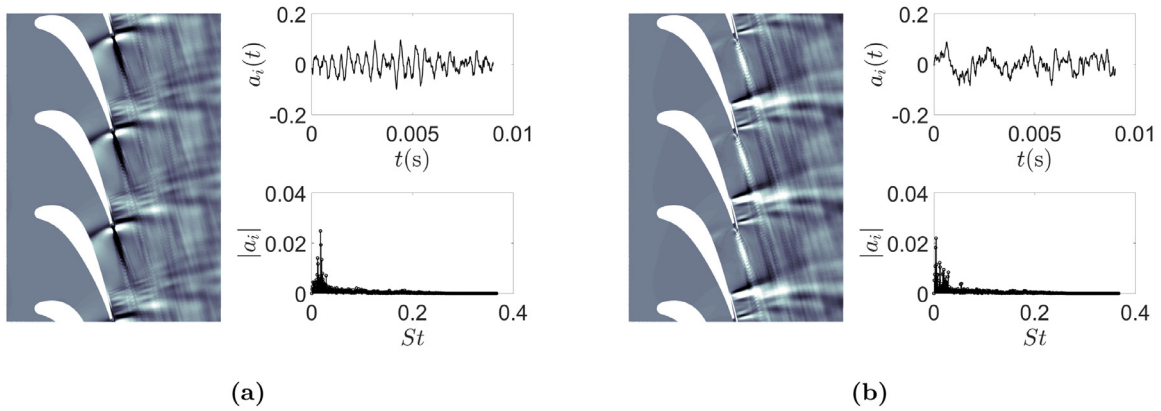
(a)   (b)

Fig. 15. Third (a) and fifth (b) POD mode of the temperature fluctuation field T'; baseline case $T_1 = 303.15$ K.

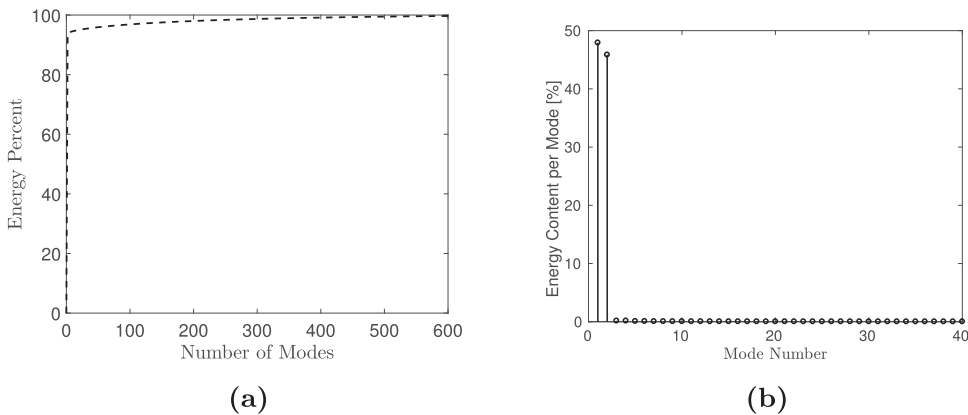(a)   (b)

Fig. 16. Cumulative energy percent retaining the first 600 modes (a), and energy associated to each mode (b). Temperature fluctuation field T'; forced inlet temperature $T_1 = 303.15$ K.

The following couple of modes $3 - 4$ is instead associated with the system of compression and expansion waves arising from the trailing edge. One could notice, in fact, the dark and light areas around the trailing edge in Fig. 15a. The frequency content is around $St_s = 0.016$ corresponding to a frequency $f_s = 2180$ Hz.

The couple $5 - 6$ is also associated with the shock movement mechanism but with a lower frequency content at $St = 0.004$ corresponding to $f = 545$ Hz, Fig. 15b. The frequency content of the shedding is well separated from the shock movement [14], since there are no topo-modes which are associated to chrono-modes with both frequencies. The frequency content of the modes representing the waves travelling at the end of the blade are not always associated to a single frequency, and even if dominant tones are distinguishable, several other frequencies appear in the temporal signal.

3.2.4. POD analysis, temperature field at forced inlet conditions

Moving the attention to the forced cases, the situation changes significantly: almost the totality of the energy is associated with the first two modes, which contain more than 90% of the energy. The cumulative energy retained as function of the number of modes and the energy per mode are pictured in Fig. 16.

The topo-mode associated with the first POD mode and its respective chrono-mode are shown in Fig. 17. The results are similar for the second POD mode. The time signal shows a perfectly periodic trend of the temporal coefficient associated with the single frequency of $f_1 = 1000$ Hz. The spectrum of the temporal coefficient, in fact, shows the dominant tone at $St_1 = 0.00733$. The spatial modeshape also shows the incoming planar wave train of entropy waves which get strongly distorted as they approach the vane passage. The aforementioned topo-mode has strong resemblances with the instantaneous temperature field of Fig. 3a, only missing the mixing feature caused by the vortex shedding.

The other modes calculated with the POD algorithm are associated to the vortex shedding phenomenon and to the shock movement mechanism. Their modeshapes are similar to the ones showed for the baseline case and are not repeated. For the temperature fluctuations, almost all the energy is contained in the first couple of modes $1 - 2$. This is true for all inlet temperatures. In Fig. 18, it is possible to visualize the modeshapes for all inlet temperatures; the chrono-mode is not presented since it is only a pure sinusoidal function at 1000 Hz. The modeshapes are very similar, with incoming waves of
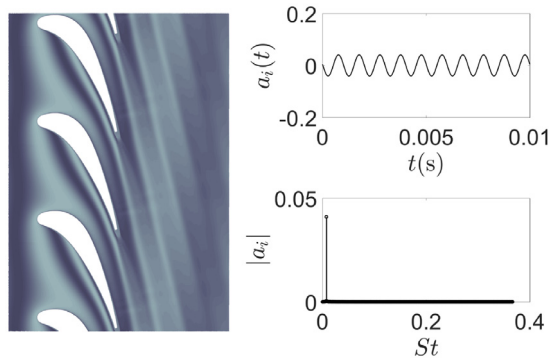
Fig. 17. First POD mode of the temperature fluctuation field T'; forced inlet temperature $T_1 = 303.15$ K.
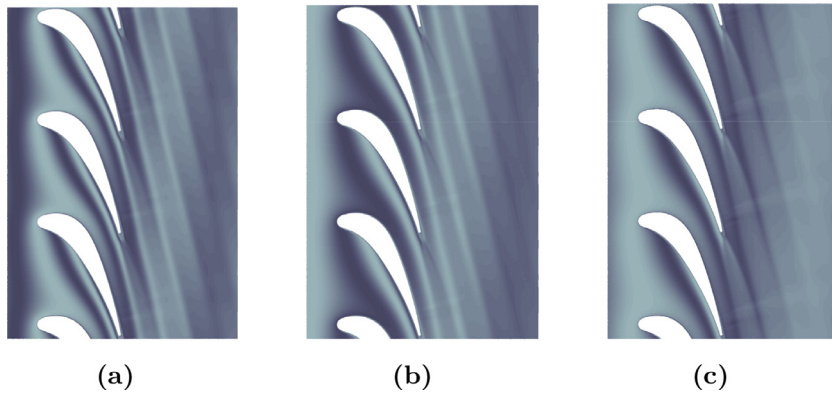

(a)   **(b)**   **(c)**

Fig. 18. First POD topo-mode, temperature fluctuation field; forced inlet temperature $T_1 = 303.15$ K (a), $T_1 = 600$ K (b) and $T_1 = 900$ K (c).

larger wavelength and a thicker wake region as the inlet temperature increases. In conclusion, the POD temperature modes, at all forced conditions, are entirely dominated by the presence of the sinusoidal forcing at f_1.

4. Effects of the incoming disturbances

From the previous analyses, it is then possible to draw important conclusions on the effect of the inlet reference temperature.

It has an effect on changing the wavelength of the incoming disturbances λ_s, which is also propagated downstream of the blade, making it thicker as the inlet temperature increases. The Strouhal numbers associated to the shedding frequency are almost constant for the two inlet temperatures of $T_1 = 303.15$ K to $T_1 = 600$ K, with their respective values of 0.176 and 0.173. While it decreases down to 0.16 for the inlet temperature of $T_1 = 900$ K.

The amplitude fields of the Fourier transform show a particular zone of interest on the suction side of the blade, towards its end. This feature is present for all forced simulations, with an outburst region of very high amplitudes (≥ 160 dB) for the highest temperature $T_1 = 900$ K.

From the POD of the temperature field, all the temporal signals of the chrono-modes associated with the inlet forcing frequency show a purely sinusoidal trend similar to the one in Fig. 16. The associated topo-modes show very similar resemblances to their respective instantaneous fields in Fig. 3. The POD algorithm for the pressure fluctuation field, on the other end, is not identifying coherent structures at a single temporal frequency as the inlet temperature increases. In fact, single topo-modes are linked, in their frequency content, to both vortex shedding, at frequency f_s, and to the movement of compression and expansion waves towards the end of the blade, at frequency f_1. The importance of the modes related to f_1, anyway, is enhanced for higher temperatures: they can represent up to 25% of the total energy of the field p' by themselves (as in the case for $T_1 = 900$ K). In all simulations, similar POD topo- and chrono- modes appear when a fluctuating temperature is imposed at the inlet. The presence of such structures in the baseline case is not evident.

It can be concluded that additional acoustic power is created in all cases where the inlet temperature field is forced at 1000 Hz. The forcing is also able to excite the movement of compression and expansion waves emitted from the trailing edge.

5. Comparisons with the analytical model

5.1. Analytical model description

The actuator disk model was first introduced in 1977 by Cumpsty and Marble [10]; it is also possible to find an accurate analytical description in the work of Leyko et al. [11], related to the indirect combustion noise generated by planar entropy waves, in a subsonic stator blade-row.

The model is based on the compact assumption, i.e. the wavelength of the disturbances, λ_s, is much larger than the reference axial chord, C_{ax}. The full entropy perturbation can be written in a non dimensional form, for small amplitudes, as

$$\frac{s'}{c_p} = \frac{T'}{T} - \frac{\gamma - 1}{\gamma}\frac{p'}{p},$$
(2)

where the primed quantities s', T' and p' are respectively the local entropy, temperature and pressure fluctuations, while the unprimed quantities represents instead their local mean value. The thermodynamic quantities c_p and γ are the specific heat at constant pressure and the specific heat ratio. The original model is extended to series of stator-rotor blade rows, the present work only deals with a single stator NGV passage.

The hypotheses of the model are summarized as follows:

- Compact assumption, $\lambda_s \gg C_{ax,\text{mid}}$.
- Low blade pitch-chord ratio, the blade details can be neglected and only the inlet and outlet flow Mach numbers and directions need to be considered.
- Subsonic axial flow.
- Radial variations are neglected, the flow is treated as two-dimensional in the axial-tangential plane.
- The acoustic power is calculated neglecting any discontinuity downstream of the turbine.
- When entropy waves interact with the turbine stage, arising pressure waves are propagated from the row upstream and downstream.
- Vorticity waves are only convected downstream.

Each flow-state, upstream and downstream, is steady, with a uniform state characterized by a flow velocity **w**, a flow direction θ, a uniform pressure p and a density ρ. Three of the four conditions are given by conservation of entropy, continuity of mass-flow and conservation of total enthalpy. For the present study the fourth matching condition is the one corresponding to the presence of a sonic throat across the NGV passage. Following the work of Leyko et al. [11] the reflection and transmission acoustic coefficients for forced planar entropy waves are expressed in terms of the flow Mach number M, the flow direction θ and the ratio of specific heats γ. They are defined as:

$$\frac{w_1^-}{w_1^s} = -\frac{1}{2}\left[\frac{\gamma-1}{2} + \frac{\cos\theta_1}{M_1} + \frac{\sin\theta_1\tan\theta_1}{\eta_1 M_1(1-M_1^2)}\right]^{-1},$$
(3)

for the reflection coefficient, where $\eta = (1 + (\gamma-1)M^2/2)^{-1}$, and

$$\frac{w_2^+}{w_1^s} = \frac{1 - \frac{1}{M_1\cos\theta_1}}{1 + \frac{1}{M_2\cos\theta_2}}\frac{w_1^-}{w_1^s},$$
(4)

for the transmitted one. The variables $w^\pm$ are used to refer to the transmitted (+) and reflected (-) acoustic waves. While the variable w^s identifies the entropy wave. The underscripts 1 and 2 finally denotes the upstream and downstream sections of the blade row, respectively.

5.2. Comparisons

The results of the analytical models are applied to the current topology of the NGV passage.

The supersonic discharge Mach number is chosen to be equal to $M_2 = 1.05$ (just above sonic conditions) in order to apply the analytical model with supersonic discharge. For fixed Mach numbers $M_1 = 0.15$, $M_2 = 1.05$ and specific heat ratio $\gamma = 1.4$, the reflection (3) and transmission (4) coefficient of the acoustic wave are now plotted as function of the incoming and discharge directions of the flow, i.e. θ_1 and θ_2.

As it can be seen from Fig. 19b, the reflected wave only depends on the inflow angle θ_1. The red dot highlights the coefficient for the geometry adopted in the simulations, i.e. $\theta_1 = 0$. For the transmitted wave, instead, the results depends on both incoming and discharge directions. Fig. 19a show the results of the analytical model. Again the red dot refers to the actual geometry of the study, with $\theta_2 = 75$. The value of the transmission coefficient is $w_2^+/w_1^s = 0.088$, while the reflection one is $w_1^-/w_1^s = 0.073$.

These results are now compared with the ones from the LES. The calculation of the acoustic coefficients was performed on two planes orthogonal to the $x-$axis, respectively at $x/C_{ax,\text{mid}} = -0.65$ upstream and at $x/C_{ax,\text{mid}} = 2.40$ downstream of the leading edge of the blade. The location $x/C_{ax,\text{mid}} = 0.0$ corresponds to the leading edge of the blade. The upstream plane is referred as plane 1, while the downstream plane is labeled as plane 2. Flow variables were sampled on the planes of interest by the means of 75 local probes. The flow quantities were also averaged in the spanwise-direction.
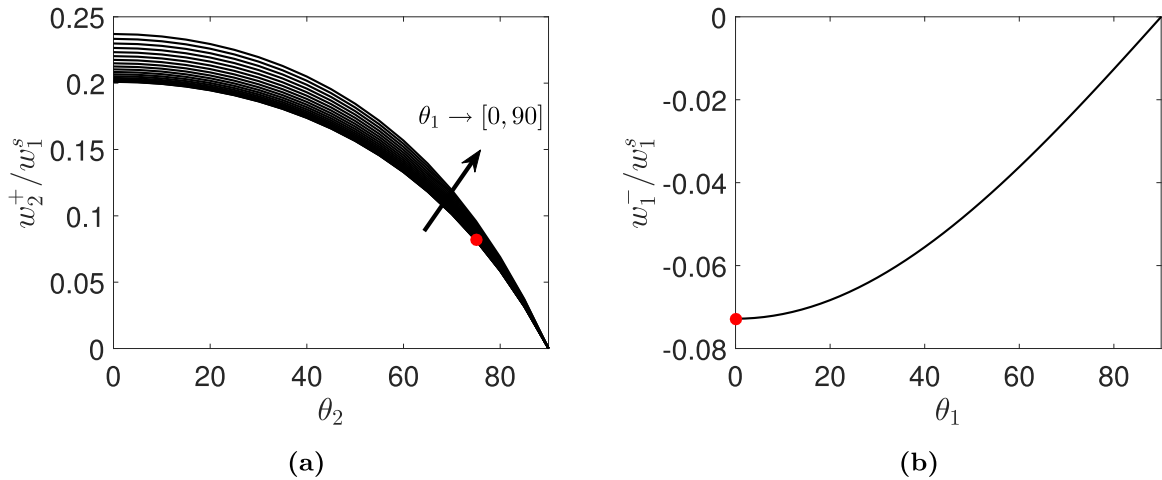
Fig. 19. Transmitted (a) and reflected (b) acoustic waves generated by an incoming entropy wave as function of the model parameters; (━) analytical model, (●) actual geometry.
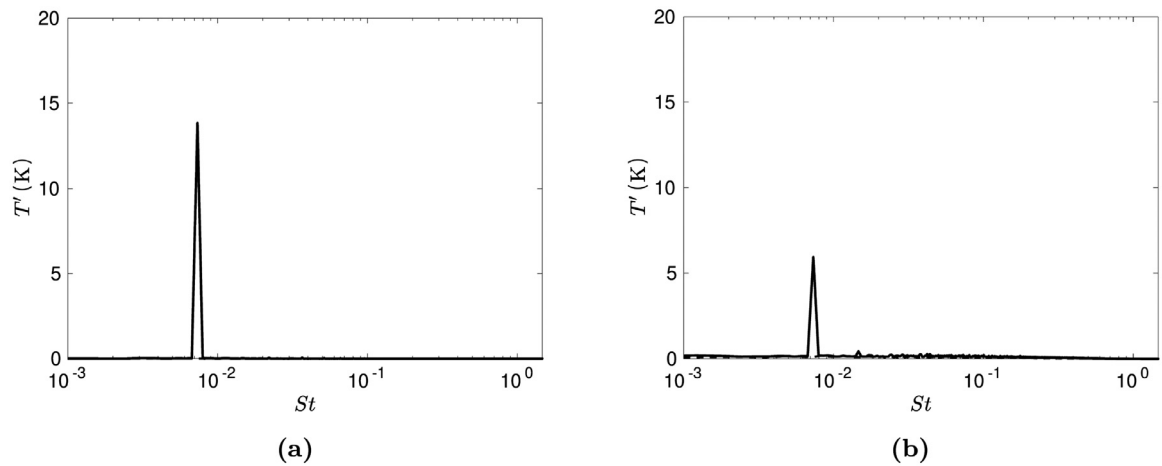

Fig. 20. Average spectrum of the forced temperature wave at plane 1 (a) and at plane 2 (b); (- -) baseline case $T_1 = 303.15$ K, (━) forced case $T_1 = 303.15$ K.

5.3. Frequency content features

Starting from the spectrum (over all probes) of the temperature fluctuation field on plane 1, from Fig. 20a it is possible to identify a peak at $St_1 = 0.00733$ for the forced case. Its amplitude corresponds to 4.8% of the inlet static temperature, as expected. No comparable amplitudes, instead, were found for the baseline case. On the other hand, for plane 2, it is possible to see from Fig. 20b, that the entropy wave is attenuated downstream of the blade, while the greatest amplitude in the entire spectrum is still registered for St_1.

Fig. 21 shows instead the pitchwise character of these waves on their respective upstream and downstream planes. The pitchwise location is normalized by the blade to blade distance H, and goes from the lower periodic boundary $y/H = 0$ to the upper periodic boundary $y/H = 1$. Again, for the baseline case, no comparable amplitudes are found also in the pitchwise distribution. The entropy wave is perfectly planar in the upstream part. This can be expected since the flow is completely uniform in this region. Instead, the wave loses its perfectly planar character on the plane downstream of the NGV passage. Once more, it is possible to see that the amplitude of the entropy waves is reduced on plane 2.

Moving to the *SPL*, spectra upstream and downstream of the blade are presented in Fig. 22. It is possible to see the presence of a tone at forcing frequency St_1 on both planes. This time, in contrast with the temperature field, it is possible to observe the presence of low frequency contents even for the baseline case. Similarly to Fig. 21, the pitchwise character of the pressure waves on the respective upstream and downstream planes is shown in Fig. 23, in terms of *SPL*.

In accordance to the results of the temperature field, pressure waves are also planar upstream of the vane, due to the uniformity of the flow. In Fig. 23a it is possible to visualize the additional acoustic power generated in the upstream plane for the forced inlet conditions. In fact, the difference in *SPL* (ΔSPL) between the baseline and the forced case is ≥ 20.
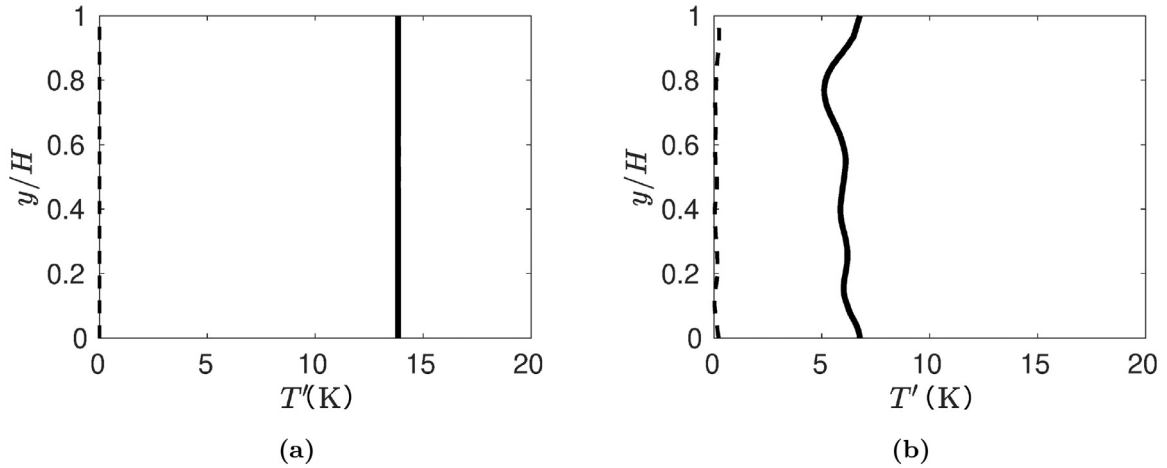
Fig. 21. Pitchwise distribution at the frequency St_1 of the temperature wave amplitude at plane 1 (a) and at plane 2 (b); (_ _) baseline case $T_1 = 303.15$ K, (___) forced case $T_1 = 303.15$ K.
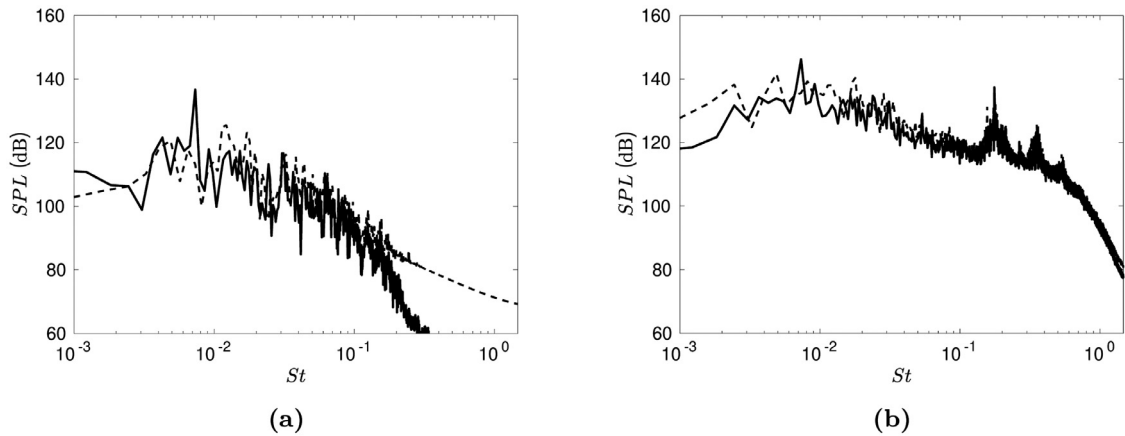

Fig. 22. Average spectrum of the SPL at plane 1 (a) and at plane 2 (b); (_ _) baseline case $T_1 = 303.15$ K, (___) forced case $T_1 = 303.15$ K, reference pressure $p_{\text{ref}} = 20$ μPa.
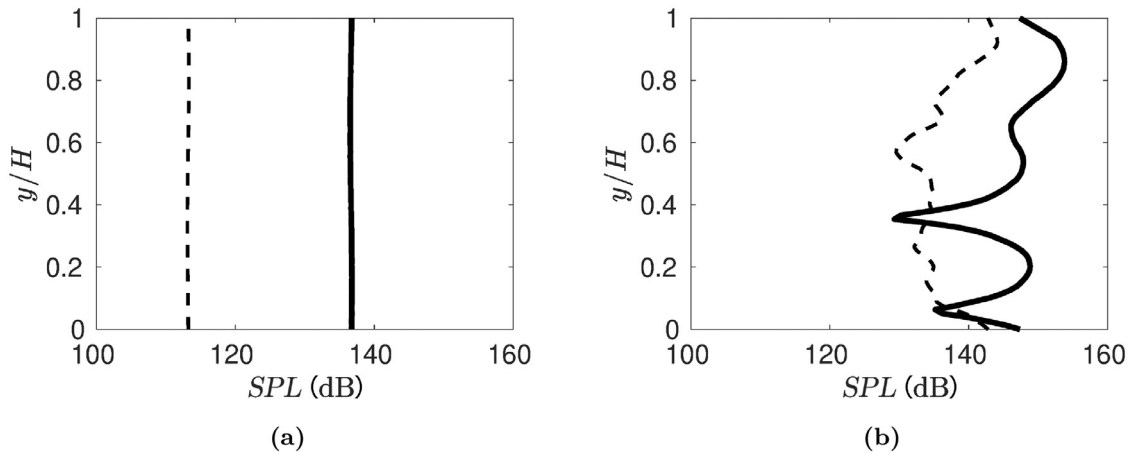

Fig. 23. Pitchwise distribution at the frequency St_1 of the SPL at plane 1 (a) and at plane 2 (b); (_ _) baseline case $T_1 = 303.15$ K, (___) forced case $T_1 = 303.15$ K, reference pressure $p_{\text{ref}} = 20$ μPa.
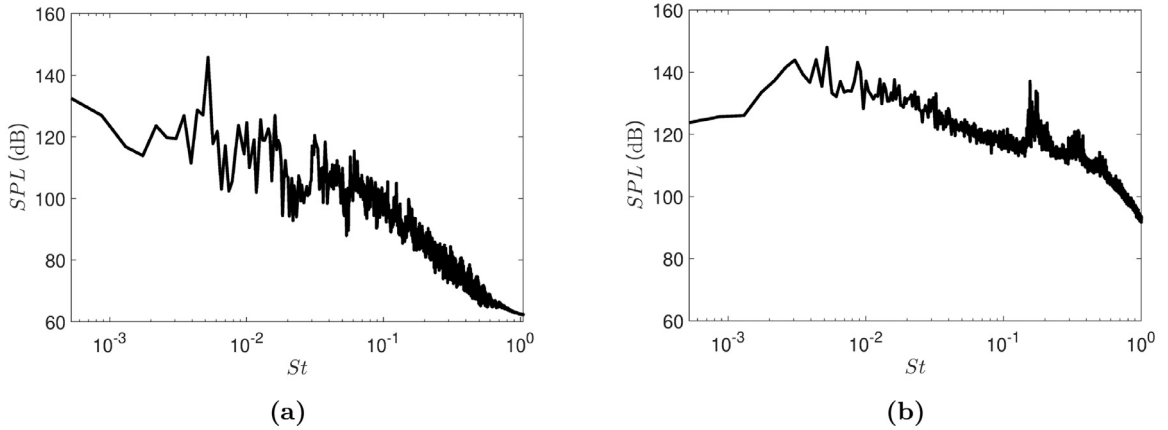
Fig. 24. Average *SPL* spectrum at plane 1 (a) and at plane 2 (b), forced case $T_1 = 600$ K, reference pressure $p_{\text{ref}} = 20$ μPa.
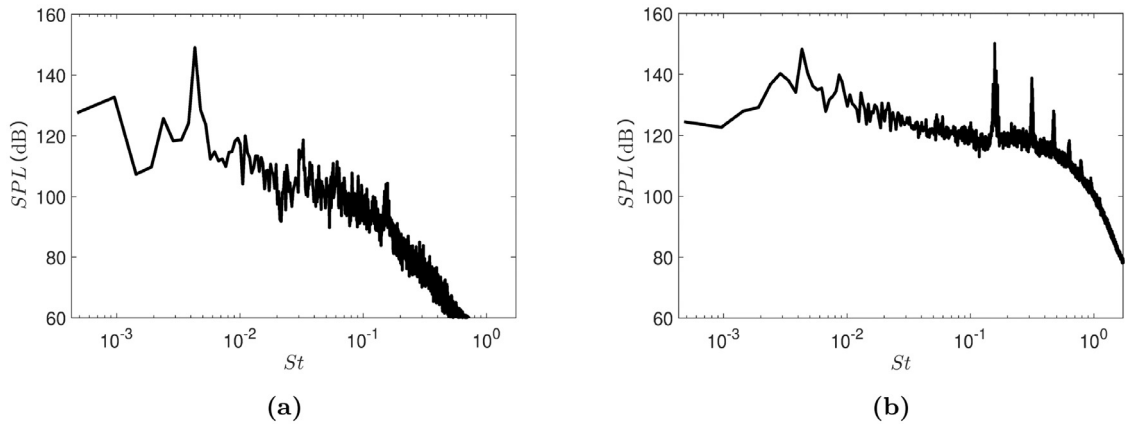

Fig. 25. Average *SPL* spectrum at plane 1 (a) and at plane 2 (b), forced case $T_1 = 900$ K, reference pressure $p_{\text{ref}} = 20$ μPa.

Additional acoustic power is also generated downstream of the passage as it can be seen from Fig. 23b. However, in this case, the acoustic wave is far from planar, with the presence of dark zones, which are also visible in the amplitude field of the Fourier Transform in Fig. 4b. Differences in $\Delta SPL \geq 15$ are also registered on plane 2.

The upstream and downstream spectra of the pressure fluctuation field are shown in Figs. 24, 25 for the two temperatures of 600 K and 900 K respectively. Two peaks are present both upstream and downstream of the passage at the respective frequency identified by St_1. Notable amplitudes at the low frequency range are still present for both temperatures, even for the baseline case.

5.4. Outcomes

At this point, after having shown the presence of an additional generated acoustic source, the analytical model is compared with the results of numerical simulations. For the coefficients of the analytical model, the parameter γ as a minor influence on the results, therefore only one value is reported. The expression used for the entropy and the acoustic waves are

$$w^s = \frac{s'}{c_p}, \tag{5}$$

$$w^\pm = \frac{p'}{\gamma p}, \tag{6}$$

where w^s and $w^\pm$ are respectively the entropy and the acoustic waves.

The amplitude of this coefficient is averaged over the plane of interest in order to get a single coefficient at a specific frequency. The final results are compared in Table 3.

The value of the transmitted entropy wave w_2^s/w_1^s is less then unity for all simulated cases, but it increases as the inlet temperature T_1 increases. Three reasons might be: first the compact assumption does not hold for the simulated cases

Table 3

Acoustic/Entropy wave coefficients.

T_1, K	f_1, Hz	St_1	$\lambda_s/C_{ax,\mathrm{mid}}$	w_1^-/w_1^s	w_2^+/w_1^s	w_2^s/w_1^s
303.15	1000	0.00733	0.76	0.011	0.068	0.45
600.00	1000	0.00524	1.11	0.032	0.075	0.50
900.00	1000	0.00431	1.36	0.047	0.084	0.51
Analytical Model	–	–	$\to \infty$	0.073	0.088	1.00

and therefore the results are not in accordance with the analytical model; second, there might be, in transonic conditions, sources of losses which do not verify entropy conservation across the vane passage; third, mixing plays an important role, smearing the intensity of the imposed wave-train, thus lowering the peak of the transmitted wave.

For the acoustic reflected coefficient w_1^-/w_1^s, instead, the value increase monotonically for higher wavelengths. This aspect suggest that, moving towards higher ratios of $\lambda_s/C_{ax,\mathrm{mid}}$, the entropy-to-acoustic conversion is enhanced across the vane. The coefficients are also in closer agreement with the analytical model, which is based on the compact assumption.

Finally, for the transmitted acoustic coefficient w_2^+/w_1^s, its value increases again monotonically for higher wavelengths. For the simulated transonic conditions, there might be flow features which interacts stronger with the system of incoming entropy waves, as the inlet temperature T_1 increases. A good example is the interaction with the system of compression and expansion waves that are emitted from the trailing edge, shown in Fig. 5. In this case, one can observe that the transmitted acoustic wave associated to the largest T_1 is close to the value predicted by the analytical model, despite the isentropic model conditions not applying for the simulated cases. As the T_1 would be further increased, it might be possible that this coefficient becomes even greater, underlining additional generated noise in transonic/supersonic conditions.

6. Conclusions

The indirect combustion noise generation mechanism has been addressed by the means of 3D LES for a simplified Nozzle Guide Vane passage of a high pressure turbine. The solver adopted for the simulations was first validated against experimental data available for off-design transonic conditions without temperature forcing in a previous paper.

In the core part of the present work, a pulsating entropy wave-train was imposed at the inlet of the domain to simulate temperature non-uniformities coming from the combustion chamber.

At the forcing frequency imposed at the inlet, several zones of the fluid domain respond with high amplitudes of the pressure fluctuations. The response of the NGV passage is stronger as the wavelength λ_s of the incoming disturbances is increased. Moreover, this aspect is complemented by the analysis performed via the Proper Orthogonal Decomposition method: the baseline case did not show any particular coherent structure at the inlet forcing frequency f_1, St_1; while pressure and temperature fields of the forced cases all showed the presence of high energy modes at that particular frequency.

The combination of the POD topo- and chrono-modes was in accordance with the flow-field results identifying the movement of compression and expansion waves emitted from the trailing edge. For the pressure fluctuation field, the chrono-modes identified the characteristic frequency content, while the topo-modes identified the zones with highest response of the fluctuation.

Reflection and transmission coefficients are compared to analytical models available in literature. The 3D simulations show that the entropy waves are highly distorted by the passage and lose their strength; this can be addressed from the entropy wave transmission coefficient which is reduced significantly for all the wavelengths of the incoming disturbances. The hypothesis of entropy conservation assumed by the analytical model might not hold in the case of transonic/supersonic conditions and with short incoming entropy waves.

The reflected acoustic wave, instead, is weaker than the one predicted by the compact theory for all simulations. However, the reflected acoustic coefficient increases towards the analytical one as T_1 increases. Finally, the transmitted acoustic wave is in fairly good agreement with the analytical model, and the transmission coefficient assumes also larger values for the higher T_1, suggesting the presence of flow features, in transonic conditions, which might generate additional noise.

A strong example is the dynamics of the compression/expansion waves emitted from the trailing edge, which interacts with the incoming entropy waves; i.e. the blade acoustic response is strongly influenced by the excitement of a latent low frequency dynamics when the planar entropy waves at 1000 Hz are imposed at the inlet. The present work highlights the features of this peculiar mechanism, which, in transonic conditions, might additionally contribute to the generated noise rather than the only one predicted by isentropic analytical models.

Declaration of Competing Interest

The authors declare that they have no known competing financial interests or personal relationships that could have appeared to influence the work reported in this paper.

CRediT authorship contribution statement

Alessandro Ceci: Software, Validation, Formal analysis, Investigation, Writing - original draft, Visualization. **Romain Gojon:** Conceptualization, Validation, Investigation, Resources, Writing - review & editing, Supervision. **Mihai Mihaescu:** Conceptualization, Supervision, Project administration, Writing - review & editing.

Acknowledgements

References

[1] S. Candel, Analytical studies of some acoustic problems of jet engines, 1972 Ph.D. thesis.
[2] F.E. Marble, S. Candel, Acoustic disturbances from gas non uniformities convected through a nozzle, J. Sound Vibr. 55 (2) (1977) 225–243.
[3] F. Backe, U. Michel, I. Rohle, Investigation of entropy noise in aeroengine combustors, J. Eng. Gas Turbines Power 129 (2007) 370–376.
[4] M.S. Howe, Indirect combustion noise, J. Fluid Mech. 659 (2010) 267–288.
[5] S. Goh, A. Morgans, Phase prediction of the response of choked nozzles to entropy and acoustic disturbances, J. Sound Vibr. 330 (2011) 5184–5198.
[6] I. Duran, S. Moreau, Solution of the quasi-one-dimensional linearized euler equations using flow invariants and the magnus expansion, J. Fluid Mech. 723 (2013) 190–231.
[7] L. Magri, J. O'Brien, M. Ihme, Compositional inhomogeneities as a source of indirect combustion noise, J. Fluid Mech. 799 (2016).
[8] F. Bake, C. Richter, M. Mühlbauer, N. Kings, I. Röhle, F. Thiele, B. Noll, The entropy wave generator (EGW): a reference case on entropy noise, J. Sound Vibr. 326 (2008) 574–598.
[9] W. Polifke, C. Paschereit, K. Döbbeling, Constructive and destructive interference of acoustic and entropy waves in a premixed combustor with a choked exit, Int. J. Acoust. Vibr. 6 (2001) 135–146.
[10] N.A. Cumpsty, F.E. Marble, The interaction of entropy fluctuations with turbine blade rows; a mechanism of turbojet engine noise, Proc. R. Soc. 357 (1690) (1977) 323–344.
[11] M. Leyko, I. Duran, S. Moreau, F. Nicoud, T. Poinsot, Simulation and modeling of the waves transmission and generation in a stator blade row in a combustion-noise framework, J. Sound Vibr. 333 (2014) 6090–6106.
[12] F. Bake, P. Gaetani, G. Persico, L. Neuhaus, K. Knobloch, Indirect noise generation in a high pressure turbine stage, in: 22nd AIAA/CEAS Aeroacoustics Conference, 2016.
[13] T. Yasa, G. Paniagua, J. Fridh, D. Vogt, Performance of a nozzle guide vane in subsonic and transonic regimes tested in an annular sector, in: ASME Turbo Expo 2010: Power for Land, Sea, and Air, American Society of Mechanical Engineers, 2010, pp. 1457–1467.
[14] A. Ceci, R. Gojon, M. Mihaescu, Large eddy simulations for indirect combustion noise assessment in a nozzle guide vane passage, Flow Turbul. Combust. (2018), doi:10.1007/s10494-018-9964-9.
[15] L. Sirovich, Turbulence and the dynamics of coherent structures. I. Coherent structures, Q. Appl. Math. 45 (3) (1987) 561–571.